Applications in Energy and Combustion Science 24 (2025) 100375

Contents lists available at ScienceDirect

Applications in Energy and Combustion Science

journal homepage: www.sciencedirect.com/journal/applications-in-energy-and-combustion-science

Coupled thermal runaway and combustion modeling for NMC811 Li-ion batteries safety: development and validation

Antonio García, Carlos Micó, Javier Marco-Gimeno *, Imad Elkourchi

CMT - Clean Mobility and Thermofluids, Universitat Politècnica de València, Camino de Vera s/n, 46022 Valencia, Spain

ARTICLE INFO

Keywords:
Process safety
Combustion kinetics
Gas venting
Safety system design
Mechanism reduction

ABSTRACT

Industrial lithium-ion battery deployment poses significant process safety risks due to thermal runaway events causing catastrophic fires and toxic gas releases. Accurate combustion modeling is essential for quantitative risk assessment and safety system design. This work presents a validated framework for process safety engineering applications. Accelerating rate calorimetry experiments were conducted on cylindrical cells of 18,650 format and NMC811 chemistry under inert and reactive atmospheres, capturing temperature profiles, pressure evolution, and gas compositions. Significant differences in vented gas mixtures were observed, with CO2, CO, and H_2 as dominant species. These results evaluated five combustion mechanisms: one for battery gas combustion, GRI-Mech 3.0, ANSYS Model Fuel Library and two-step global models. Homogeneous reactors and laminar flame speed simulations were used for evaluation. Detailed mechanisms produced consistent ignition delay and flame propagation results, while simplified models showed deviations. A mechanism reduction is presented, down-scaling to 128 species and 794 reactions (80 % reduction) without compromising accuracy. This reduced mechanism was integrated into a 2D axisymmetric CFD model incorporating TR, gas venting, and combustion processes. The model accurately reproduced temperature rise, pressure development, and venting dynamics. The work provides a validated reduced kinetic mechanism for battery gas combustion that can be used to enhance safety of battery module during design processes.

1. Introduction

The increasing integration of lithium-ion batteries (LIBs) into electric vehicles, grid-scale storage, and portable electronics has raised new concerns for process safety and risk engineering. While LIBs offer high energy density and performance, they also pose critical hazards, especially in industrial and storage environments, due to the potential for thermal runway (TR) and associated fire and explosion risks. In the context of chemical process safety, TR presents a worst-case failure mode involving self-accelerating exothermic reactions, toxic gas release, and flame propagation, which can lead to catastrophic scenarios if not properly understood and mitigate [1,2].

Thermal runaway typically initiates due to internal short circuits, mechanical damage, overcharging, or external heating, leading to the decomposition of battery components and the release of flammable gases such as hydrogen ($H2$), carbon monoxide (CO), methane (CH_4), ethylene (C_2H_2), and various organic carbonates [3,4]. The composition and volume of these gases are highly dependent on battery chemistry and state of charge (SOC), with high SOC cells exhibiting more exothermic behavior and richer gas mixtures. Accurate prediction of these gas compositions and their combustion characteristics are essential for industrial fire suppression system design, emergency ventilation calculations, and toxic exposure assessment. Ignition of these gases, either via auto-ignition or external spark, can cause flames that feed heat back to neighboring cells, intensifying the thermal response and promoting Thermal Runaway Propagation in battery energy storage systems and manufacturing facilities [5,6]. While conventional TR models predominantly focus on internal exothermic reactions and heat transfer within cells, the role of combustion in accelerating or modifying TR events has been underrepresented when characterizing the battery failures, hence underrepresenting the catastrophic consequences on people and facilities from these events. Recent studies underscore the importance of modeling combustion processes alongside venting and TR dynamics for a more accurate prediction of battery fire hazards [7,8]. The interaction between vented gases and ambient air, especially under confined or semi-confined conditions, leads to complex thermodynamic and kinetic phenomena, such as turbulent mixing, pressure build-up, and localized flame propagation [9]. To support safety design and risk

* Corresponding author.
E-mail address: jamargi2@upv.edu.es (J. Marco-Gimeno).

https://doi.org/10.1016/j.jaecs.2025.100375
Received 31 July 2025; Received in revised form 12 August 2025; Accepted 22 August 2025
Available online 23 August 2025

mitigation, combustion models must accurately reproduce these dynamics within computationally feasible frameworks, especially when used in CFD simulations of real-world battery fire scenarios. These processes demand multi-physics models that combine cell degradation, gas-phase transport, and combustion kinetics to capture real-world fire scenarios accurately. Recent studies have also explored thermal runaway propagation, vent gas ignition, and safety implications in lithium-ion systems. For instance, Xie and Zhang [10] demonstrated how state of charge significantly affects ignition risk and gas reactivity in large-format prismatic cells. Li et al. [11] examined how the trigger location influences propagation speed and thermal severity, while Lin et al. [12] compared combustion behavior in LIBs with liquid and semi-solid electrolytes under TR. Other studies, such as the one carried out by Wang et al. [13] analysed the flame (laminar flame speed, explosion limits) under controlled conditions, employing characteristic gas composition from LIB vented gases. These studies highlight the relevance of combustion modeling to battery fire risk but often rely on simplified kinetics or analyze TR and combustion in isolation.

Furthermore, Wang et al. [14] demonstrated that overhead fire exposure accelerates thermal runaway propagation in battery racks due to enhanced heat transfer in confined spaces. Xu et al. [15] investigated TR propagation and gas generation in NCM622 modules at varying states of charge (SOC), confirming that higher SOCs lead to greater vented gas volume and faster propagation, which directly informs battery pack design and hazard zoning. The effect of TR propagation through fire radiation is further explored by Wang et al. [16], determining the needed heat transfer to trigger the fire event. Working conditions of the cell can also affect the TR event and the deduced fire. For example, Xie et al. [10] identified critical SOC-dependent thresholds for deflagration risk, essential for explosion protection measures. Jie et al. [17] expanded this by comparing TR behavior across multiple trigger modes, showing that combined abuse significantly increases combustion severity and risk. Meanwhile, Dong et al. [18] focused on pressure-driven deformation during TR, demonstrating how internal pressure buildup can compromise module integrity insightful for mechanical containment strategies. Fan et al. [19] numerically analyzed deflagration and suppression in LIB vent gas combustion, providing practical guidance for pressure relief and extinguishing strategies.

In this context, selecting appropriate chemical kinetic mechanisms is central to accurately model combustion that could be applied to enhance the safety of battery technologies during the design phase. The mechanism from Lund University, recently developed by Nilsson et al. [20], combines detailed sub-mechanisms to represent hydrogen, hydrocarbons, carbon oxides, and fluorinated compounds found in Li-ion vent gases. It strongly agrees with experimental laminar flame speeds and ignition delay times across representative gas mixtures. However, including hundreds of species and thousands of reactions significantly increases computational cost, limiting its use in high-dimensional CFD simulations. In contrast, the GRI-Mech 3.0 mechanism, a widely used kinetic model optimized for natural gas combustion, has been adopted in early battery combustion studies for its balance of complexity and computational efficiency [21]. Nevertheless, it lacks reactions for fluorinated and carbonate species, compromising accuracy for battery-specific applications, particularly under high CO_2 dilution conditions [4]. Commercial tools like the ANSYS Model Fuel Library offer pre-validated surrogate mechanisms, but they often omit toxic byproducts such as HF and PF_6, thus requiring expert calibration when applied to battery vent gases [8].

To mitigate these trade-offs, reduced mechanisms have gained attention on other combustion applications. These involve systematically eliminating less influential species and pathways while preserving the core reaction dynamics. For instance, Yu et al. [5]. and Cellier et al. [22] have developed reduced models (with as few as 17–22 species) that replicate key combustion characteristics with high fidelity, facilitating efficient simulation of TR and fire scenarios in CFD environments. In contrast to all these methodologies, global one-step and two-step reaction schemes have been used as simplified representations, useful in parametric or preliminary hazard studies despite their inherent limitations in predicting pollutant formation and flame behavior under varying pressures. Such simplified mechanisms have already been used in literature to represent battery fires [23,24] and [25] under three-dimensional computational studies, and later reviewed by [26]. Some other studies have used more detailed mechanisms, such as the San Diego reaction mechanism [27] on premixed TR fires to predict the peak domain pressure and predict explosions. Furthermore, battery fire scenarios often involve elevated pressures and confined volumes that significantly influence combustion kinetics and flame propagation, and this is not properly reflected by too simplistic mechanisms. Is such the interest on understanding TR and the subsequent fires, that several studies have already been published on fire suppression techniques on several LIB applications by using novel techniques to control TR propagation and resisting derived fires, as it is the example of [28] or [29]. As indicated by Wang et al. [30], in order to predict the consequences of a TR event and eventual file, would be necessary to build a multiscale model that considers the whole span of the phenomenon, which precisely what the focus of this work is, as it will imply a tool for assessing the consequences of TR.

While recent research has advanced the understanding of thermal runaway and combustion interactions, comprehensive evaluation of combustion mechanisms ranging from detailed to reduced and global models within a coupled TR-venting-combustion framework remains limited. Previous studies have treated mainly combustion modeling isolated or used generic surrogates that are not representative of actual battery vent gases. On the other hand, studies that employed detailed mechanism were only used for premixed flames, while diffusion flames are also of important once a TR event takes place. Thus, there is a pressing need to identify combustion mechanisms that are both accurate and computationally feasible, especially under the high-pressure, mixed-gas environments typical of TR events.

To address the gap in the field of TR gas combustion process, the following specific objectives have been considered:

- Acquire high-resolution experimental data on vent gas composition and thermal behavior during thermal runaway of commercial NMC811 cells under both inert and reactive atmospheres, specifically to provide mechanism-relevant inputs for model calibration and validation in coupled combustion–thermal runaway simulations. This targeted characterization ensures direct consistency between experiments and CFD modelling
- Conduct a systematic comparative assessment of multiple combustion kinetic mechanisms for their accuracy in predicting ignition delay and flame propagation characteristics of battery vent gases.
- Develop a computationally efficient reduced mechanism that maintains high fidelity to detailed kinetics for battery vent gas combustion across various operating conditions.
- Integrate the reduced mechanism into a coupled simulation framework for thermal runaway, venting, and external combustion to validate against experimental measurements.
- Analyze the flame structure, temperature distribution, and species evolution during the coupled TR-combustion process to provide insights for battery safety design.

While previous studies have examined gas venting behavior of NMC811 cells, they have not directly integrated experimentally determined gas compositions under controlled atmospheres into a CFD workflow. The present study addresses this issue and provides novel insights into selecting combustion models for battery safety simulations. The findings aim to bridge the gap between fidelity (through combustion mechanism assessment) and efficiency (by mechanism reduction), offering guidance for researchers and engineers involved in battery fire risk modeling and mitigation strategies.

2. Materials and methods

2.1. Combustion mechanisms employed

This section details the combustion kinetic mechanisms employed in this study, ranging from detailed chemical kinetic models to simplified ones. Five distinct mechanisms were evaluated, including the Lund mechanism, GRI-Mech 3.0, ANSYS Model Fuel Library (MFL), and two-step models illustrated in Table 1.

The mechanism from Nilsson et al. [20] (Lund mechanism) is a detailed chemical kinetic model specifically developed to simulate the combustion behavior of lithium-ion battery vent gases. It combines sub-mechanisms that cover hydrogen, carbon monoxide, hydrocarbons (e.g., CH_4, C_2H_4), fluorinated species (HF), and carbonates. The mechanism is designed to handle the diverse compositions typical of vented gases during thermal runaway, including variation due to the chemistry and state of charge. It includes several hundred species and thousands of elementary reactions. The mechanism from Nilsson et al. [20], from Lund University, has been referred to as "Lund" from now on. GRI-Mech 3.0, developed by Smith et al. [31], is a widely used detailed mechanism designed for modeling the combustion of natural gas, particularly methane, as well as the oxidation of H_2 and $C0$, and the formation of NO_x. It includes 53 species and 325 elementary reactions. Although it is not specifically designed for battery gases, it serves as a reference model for small hydrocarbon and syngas-like mixtures. The ANSYS Model Fuel Library (Ansys Model Fuel Library) provides a set of validated reaction mechanisms for over 70 hydrocarbon and oxygenated fuels. It can combine these sub-mechanisms to create surrogate blends that represent battery vent gases. Global combustion models utilize simplified reaction schemes to represent the overall oxidation process of fuels. A typical one-step model assumes a single reaction:

$$Vent\ Gas\ Mixuture + aO_2 \rightarrow bCO_2 + cH_2O \tag{1}$$

With an Arrhenius reaction rate:

$$\omega = AT^n exp\left(-\frac{E_a}{RT}\right)[VentGas]^{\alpha}[O_2]^{\beta} \tag{2}$$

Two-step models introduce an intermediate species such as CO, splitting the process into partial and complete oxidation steps. These models can be tuned to replicate observed flame temperatures and propagation speeds. They are often used in preliminary hazard simulations and parameter sweeps due to their low computational demand. The global parameters (e.g., activation energy, pre-exponential factor) are typically calibrated using experimental data or a detailed mechanism [34].

2.2. Experimental methodology for model input data generation

The LIB used in this work a cylindrical NMC811 cell, with a diameter of 18 mm and a height of 65 mm. The main specifications are presented in Table 2. Experiments were carried out using the accelerating rate calorimetry model ARC THT EV+, which was manufactured by Thermal Hazards Technologies (Fig. 1). Before the ARC test starts, the cell is fully charged to 4.2 V using a constant-current and constant-voltage (CC—CV) protocol with a bidirectional current source Arbin LBT 10 V 100A 001E02582. The charging procedure begins with a constant current of 1C-rate up to the maximum voltage, according to the battery manufacturer. During the constant voltage charging phase, the current progressively decreased to 5 % of 1C-rate. After, the batteries were left to rest for 60 min (zero current) at room temperature. N-type thermocouples were used to record the temperature data during the ARC test, while the pressure data were recorded using an Agilent 34901A Datalogger. Fig. 2 shows the locations of the thermocouples.

Table 1
Summary of combustion mechanisms evaluated in this study.

Mechanism model	Type	Species	Reactions	Reference
Lund	Detailed	613	3698	[20]
GRI-Mech 3.0	Detailed	53	325	[31]
ANSYS MFL	Semi-detailed	–	–	[32]
Two-Step	Global	6	5	[33]

Table 2
NMC811 18,650 Lithium-ion cell specifications.

Parameter	Value
Nominal capacity	3.2 Ah
Nominal voltage	3.6 V
Maximum charge voltage	4.2 V
Cut-off voltage	2.5 V
Cell mass	49 g
Dimensions [mm]	18 × 65 mm
Cathode Chemistry	NMC811
Anode Chemistry	Graphite
Vent Cap holes	3
Total Electrical Energy	41.47 kJ

The experiments followed the ramp heating method to induce the sample cells into TR. In the ramp heating mode, the EV-ARC would overheat the sample from ambient temperature to 300 °C at a constant rate of 2 °C/min. The advantage of this ramp heating mode is that it can significantly reduce the duration time of the test and, at the same time decrease the TR onset temperature. The cell surface temperature, the canister internal pressure, the gas temperature inside the canister, and the canister temperature were during experiments.

The schematic diagram of EV ARC is illustrated in Fig. 1. For this test, the Li-ion battery was positioned in the center of the canister. The external plastic cover of the battery was removed. This was done to avoid that when the battery is heated in the ARC, the external plastic cover would melt and form a layer of protection, thus influencing the heat transfer. Three N-type thermocouples with a bead diameter of 1 mm were used. One attached to the battery surface at the center, the two thermocouples were located inside the canister measuring the air temperature (T_2), and one attached to the canister inside wall (T_3). Temperatures, pressure, and voltage data were recorded until the battery went into thermal runaway. The cell is inserted into a closed canister of steel, allowing the collection all gases vented during thermal runaway decomposition. In this way, analyzing its composition after the ARC test is possible. For this purpose, this work used a gas chromatograph (GC) Agilent 990 Micro by Agilent Technologies. The generated pressure within the closed-volume allows that the mixture of gases generated after the event, which is representative of what is ejected plus the components prior the TR, enter the GC column. The GC was calibrated for O_2, N_2, H_2, CO, CO_2, CH_4, C_2H2, C_2H_4 and C_2H_6. Regarding the pressure sensoring, a Kistler 4045A is employed, being set on the inner canister walls. Its position has been ensured to be located on the main gas region to avoid as possible effects of the gaseous plume on the signal capturing that could affect the collected data.

2.3. Modeling methodology

2.3.1. Zero/one dimensional models

Low level simulations have been run using CANTERA. Ignition-delay calculations have been done using homogeneous reactor. The reacting rate expression for the chemical kinetics is given by Eq. (3). Prime superscript represents forward stoichiometric coefficients, while double prime superscript represents reverse stoichiometric coefficients. χ os the chemical symbol for the k species.

$$\sum_{k=1}^{} \nu'_{ki}\, \chi_k \langle - \ - \ \rangle \ \sum_{k=1}^{K} \nu''_{ki} \chi_k \tag{3}$$

Production rate of the "k" species is given by a sum of rate of progress variables (q) involving the "k" species, as per Eq. (5):

Fig. 1. Experimental Setup with the EV + ARC, (a): CMT-UPV battery lab, (b): the setup measurement system (b).

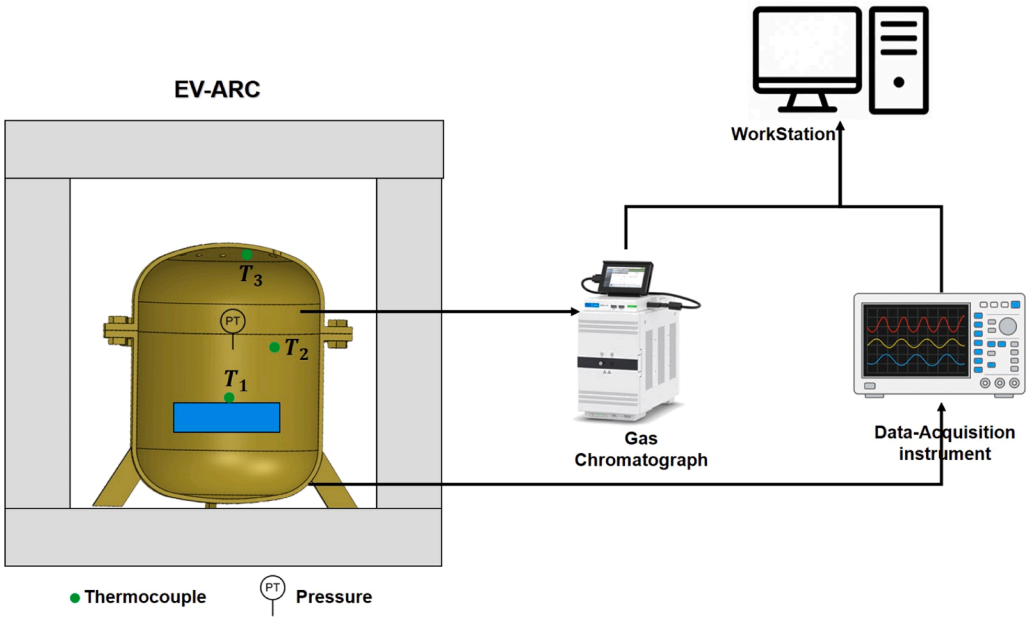

Fig. 2. Experimental setup measurement.

$$\dot{\omega}_k = \sum_i \nu_{ki} q_i \tag{4}$$

$$\nu_{ki} = \nu''_{ki} - \nu'_{ki} \tag{5}$$

The rate of progress q_i again, is dependent on the forward rate constants (k_{fi}), given by Arrhenius temperature dependence (Eq. (6)), in which the activation energy of each gas reaction, the frequency factor and the exponent β affect the kinetics.

$$k_{fi} = A_i T^{\beta_i} \exp\left(-\frac{E_a}{RT}\right) \tag{6}$$

Zero-dimensional simulations are carried out considering a perfectly mixed reactant and oxidant species, in which mass and energy conservation are ensured. One-dimensional simulations are also considered to capture laminar flame speed characteristics. This is done through a Premixed Flame Model, where finite difference methods are used to solve the governing differential equations. In them, a specific inlet velocity of 5 cm/s of premixed composition is set. The spatial domain has been discretized into a total of 500 points in a total of 3 cm. In addition to the previous equations, species transport is also solved. For that reason, these 1D simulations need of gaseous phase transport data properties.

2.3.2. *Three dimensional models*

Computational geometry has been recreated in the CFD simulation software STARCCM+. Both the cell of interest and the closed-volume geometry have been considered, in addition to the LIB holder that maintains it in place. Both the solid and gaseous phases have been spatially discretized through polyhedral elements. In the available gaseous domain, and with the aim of properly capturing the heat transfer dynamics from the external closed-volume walls to the gas mixture (and vice-versa), and the boundary layer characterization; a prismatic layer is introduced in the interfaces with the solid phase, consisting of 10 layers with a stretching factor in order to set the first near-to-wall element at a $y+$ ~1 up to $y+$~2000. Refinements are placed on the regions close to the venting cap to properly capture the venting and combustion dynamics. Radiation heat transfer is considered across the gaseous domain, for that purpose, gray thermal radiation is introduced through Participating Media Radiation. Emisivities of the canister wall (steel) have been set to 0.8 ([35,36]), while for the aluminum LIB casing, a value of 0.25 has been set [36]. As a cylindrical cell is being

employed and the geometry of the closed-volume is axis-symmetric, computational cost has been reduced by transforming the three-dimensional domain into a two-dimensional axis-symmetric geometry, hence drastically reducing the amount of computational cells. Boundary conditions have been set at the external closed-volume walls, in which the experimental temperature profile has been imposed. The venting cap of the LIB has been considered as a Mass Flow Inlet, in which the composition and mass flow rate are calculated through the procedure indicated below. Mesh quality is assessed through a mesh independence study which considers effects both from the solid (TR) and gaseous (heat up and combustion) phases. Four different base sizes have been chosen, ranging from 1.25 to 10 mm, referring to meshes of 132×10^3 to 9×10^3 elements, respectively. The TR trigger temperature, the achieved maximum pressure and temperature of the surrounding air have been used to assess the required independence. Through the mesh with characteristic size of 2.5 mm, the differences with the immediately finer mesh (1.25 mm) are less of 1.3 % in all the chosen parameters. Hence, the mesh of 2.5 mm, with a corresponding cell count of 50×10^3 has been selected for the subsequent analysis. A visual representation of the spatial discretization carried out is included in Fig. 3.

Regarding the equations driving the gaseous phase, the commonly known Navier-Stokes [37] equations are introduced for the conservation of the fluid momentum, in addition to the continuity equation for the mass conservation. To capture the temperature field around the domain, the energy conservation equation is also included. To capture the effects of the turbulence, a Reynolds-Averaged Navier-Stokes approach has been considered to model all the scales of the turbulence while maintaining relatively low the computational cost. The two-equation model from Wilcox [38] (kw-SST) has been included to address the closure problem. As one of the main purposes of the present manuscript is to recreate the combustion of the ejected gases from the LIB, a reacting flow model needs to be considered. To accurately capture the reacting flow dynamics, intermediate species and the kinetics, a reacting species transport model has been considered. In it, the transport equations of the involved combustion species are included in the model. As the mentioned combustion mechanisms are relatively complex, implying hundreds of species and reactions, the Complex Chemistry sub-model within the CFD software is employed, which provides the necessary numerical tools to resolve the combustion kinetics in an efficient way. Together with it, the Laminar Flame Concept (LFC) is used. It modifies the local turbulent diffusivity to thicken the flame and increase the flame propagation speed over the laminar value. It allows to sufficiently resolve the internal flame on the mesh through that thickening, as the physical dimensions would be lower than the minimum computational cell size. It evaluates the instantaneous reaction rate at the mean temperature, pressure and species mass fraction, being applicable to unsteady flames. Clustering techniques are employed to accelerate the numerical convergence across the whole computational domain. Through it, the chemistry kinetic solver identifies computational cells with similar thermodynamic and mass composition, and resolves the kinetics once per cluster of cells, reducing the number of calculations performed.

Regarding the solid phase, conductive heat transfer is considered. The closed volume material, together with the LIB holder and the LIB casing have been considered spatially uniform thermal properties, as they correspond to steel and aluminum. The LIB jelly-roll, on the other hand consists of a rolling of the electrode material, resulting in non-uniform thermal conductivity values. If a cylindrical coordinate system is considered in the symmetry axis, axial and tangential values should differ from the radial conductivity. A summary of the properties employed for the JR is supplied in Table 3.

In addition to the heat transfer across the solid phase, during TR, the jelly-roll can generate heat in an uncontrolled way if subjected to certain temperatures. The process of replicating this behavior will be described next. The heat generated by the TR mechanisms can be approximated as $\dot{Q}_x$, in which the x subscript relates to each one of the different reactions (exothermic or endothermic) that take place. As in a combustion model, the generated heat is given by Eq. (7). It is composed of the reacting mass m_x (kg), the enthalpy of heat H_x (J/kg), and the reaction rate κ_x (1/s).

$$\dot{Q}_x = m_x \kappa_x H_x \tag{7}$$

The reaction rate then is based on an Arrhenius expression with shape Eq. (2), which depends on the frequency factor (A_x), the activation energy ($E_{a,x}$), and the non-dimensional concentration (c_x) of the reactant of interest, with a specific exponent (m). The activation energy is indicated by E_a, being all the expression dependent on the temperature (T).

$$\kappa_x = c_x^m A_x e^{\frac{E_{a,x}}{RT}} \tag{8}$$

Additionally, the non-dimensional concentration is related to the reaction rate through Eq. (9), going from a fresh state ($c_x = 1$) to a completely burned state ($c_x = 0$).

Table 3
Jelly-Roll properties.

Parameter	Value	Reference
JR Density	2580 kg/m3	[39]
JR Specific Heat	830 J/kgK	[39]
JR Conductivity	(3.4, 28, 28) W/mK	[39]

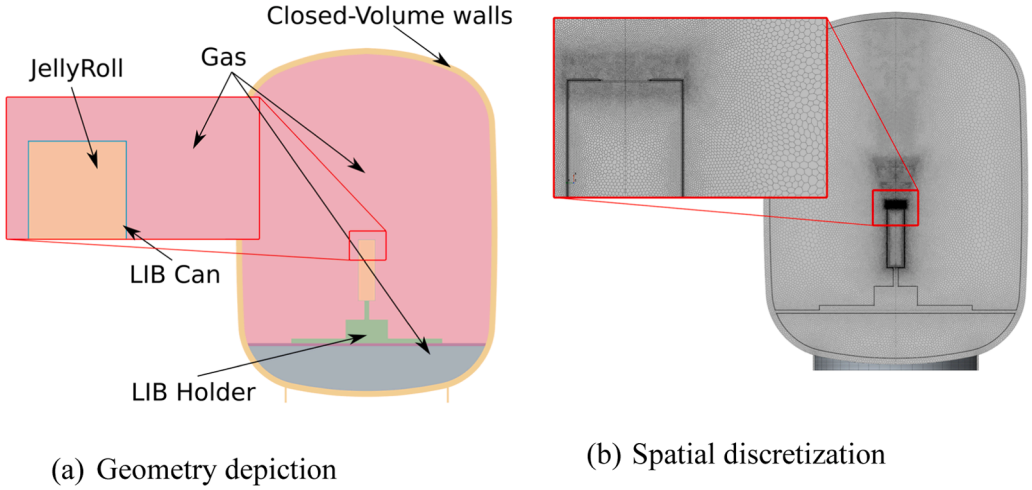

Fig. 3. Computational representation of the experimental domain.

$$\kappa_x = -\frac{dc_x}{dt} \tag{9}$$

The TR model reactions are based on the work by Ren et al. [40]., considering the TR for a NMC111 cathode cell. It considers exothermic/endothermic processes for the degradation of the SEI layer, anode, electrolyte, binder and cathode. The modifications made by García et al. [41] have been considered to adapt the mechanism to a NMC811 cell, which is the cell that is currently of interest. Additionally, the cell employed is the same that of the referenced work, hence the updated parameters are directly applicable to the present one. The exothermic model is applied to each of the individual computational cell that the JR is made of. Heat transfer effects through the JR geometry is driven by the heat transfer equation included in Eq. (10). In it, the thermal conductivity is indicated by k and the heat capacity by C_p. In the presented equation, only two dimensions are of the space are used by the CFD model. V_{cell} is the volume of the computational cell that is being considered.

$$\frac{\partial}{\partial x}\left(\frac{k\partial T}{\partial x}\right)+\frac{\partial}{\partial y}\left(\frac{k\partial T}{\partial y}\right)+\frac{\sum \dot{Q_x}}{V_{cell}}=\rho C_p\frac{\partial T}{\partial t} \tag{10}$$

In addition to the TR model, a venting model is used. In this case, the venting approach follows a 0D formulation, which will provide the inlet mass flow rate, temperature and composition into the gaseous fluid domain. The different gas generation mechanisms are known through previous work [42]. For example, SEI decomposition is responsible for the generation of carbon dioxide and ethylene, anode reaction causes the appearance of carbon monoxide and ethane. The decomposition of electrolyte is also a source of carbon dioxide, while the reaction in which the binder is present causes the presence of hydrogen. The proposed TR model accounts for the internal degradation mechanism responsible for the main gas generation pathways as described. In that way, a venting model is built based on these reactions. When the non-dimensional concentration of each reactions equals the unity ($c_x = 1$) and degradation has still not taken place, no gas should have been generated. On the other hand, if the concentration of the reaction has been totally consumed ($c_x = 0$), the degradation pathway should have generated its totality of associated gas. Through gas cromatograph techniques, the final gas composition after a ARC—HWS test can be characterized. This information is used as an input to the venting model, as it indicates the final state the gas composition should achieve. For that reason, it has been assumed a linear relationship of the generated mass with the state of degradation of the reactant c_x through Eq. (11). In it, m_x represents mass that has been generated up to a specific state based on the degree of degradation of each reactant c_x. The total mass of each individual gas component is provided through m_{final}.

$$m_x = m_{final}\left|c_x - c_{x,0}\right| \tag{11}$$

In addition to the calculation of the mass being generated, the model needs a venting mechanism. Based on the status of the TR event, the generated mass could accumulate within the cell itself, or it could be vented to the exterior. During early stages of the event, at relatively low temperatures, the vented gases accumulate in the cell, increasing the internal pressure. The gases present internally are driven by the Vapour-Liquid equilibrium of the electrolyte in the cell together with the gases generated. The vapour content of the electrolytes is considered through Antoine equation (Eq. (12)), whose parameters (A, B and C) for Dimethyl Carbonate (DMC) and Ethylene-Carbonate (EC) have been obtained in previous works, [43] and [44] respectively. A composition of 70 % DMC, 30 % EC in mass has been considered.

$$\log_{10}(P_{VLE}) = A - \frac{B}{T+C} \tag{12}$$

The partial pressure of the generated gases are obtained through ideal gas Eq. (13), and the total pressure inside the cell is obtained through the sum of all the partial pressures.

$$PV = nRT \tag{13}$$

Once the internal pressure compromises the structure of the cell, the venting cap opens, releasing the accumulated gases and the ones currently generated. To capture this second event, the Non-Vapour Liquid Equilibrium (NVLE), similar equations are considered. No further generation of electrolyte vapour has been considered, while the generation of gases is then driven by Eq. (14).

$$\dot{m_{gen,x}} = \frac{dc_x}{dt}\, m_{final,x} \tag{14}$$

Although mass is being generated, not all of it immediately leaves the LIB through the venting cap. Hence, the amount of mass present in the LIB can be calculated through Eq. (15), through a balance of what is being generated and what is being ejected ($\dot{m_2}$) and the mass fraction of the gas of interest ϕ.

$$m_x = \dot{m_{gen,x}} - \dot{m_2}\phi \tag{15}$$

The amount of gas present within the LIB will dictate the internal pressure of the LIB during NVLE through Eq. (16), accounting for the variation of mass within the cell, its average temperature T_{LIB} and the available volume inside the LIB, V_h.

$$\frac{dP_x}{dt} = \frac{RT}{V_h}\frac{dm_x}{dt} + \frac{m_x R}{V_h}\frac{dT_{LIB}}{dt} \tag{16}$$

Again, through these pressure variations, the evolution of the internal pressure can be tracked, and this internal pressure will be driving the mass flow rate of ejected gases through the venting cap, which has been characterized through isentropic flow Eqs. (17–20). Subindex 1 stands for the state of the cell variables inside the LIB, while 2 stands for the variables at the "nozzle" throat, in which maximum velocities should be achieved. A discharge coefficient C_d is introduced at Eq. (20) to account for the irreversibility of the process.

$$P_2 = \max\left(P_a, P_1\left(\frac{2}{\gamma+1}\right)^{\frac{\gamma}{\gamma-1}}\right) \tag{17}$$

$$T_2 = T_1\left(\frac{P_a}{P_1}\right)^{\frac{\gamma-1}{\gamma}}\ (Subsonic)\ |\ T_2 = T_1\left(\frac{2}{\gamma+1}\right)\ (Sonic) \tag{18}$$

$$Ma = \min\left(1, \sqrt{\left(\left(\frac{P_1}{P_2}\right)^{\frac{\gamma-1}{\gamma}} - 1\right)\left(\frac{2}{\gamma-1}\right)}\right) \tag{19}$$

$$\dot{m_2} = C_d A_v \rho_2 u_2 \tag{20}$$

3. Results and discussion

3.1. Experimental results

This section presents the results of the thermal runaway experiment conducted on the NMC811 lithium-ion cell at 100 % SOC. Fig. 4 shows the evolution of temperature and pressure throughout the experiment. The cell initially experienced a gradual temperature rise under controlled heating, followed by a sharp increase indicating the onset of thermal runaway at approximately 140 °C. This point marks the beginning of a rapid exothermic reaction, as evidenced by the steep rise in both pressure and temperature. Shortly after the TR event began, the peak cell surface temperature reached approximately 704 °C. Simultaneously, the pressure inside the sealed canister spiked to 5.70 bar, confirming substantial gas generation and eventual combustion. The combustion during this reactive atmosphere experiments was not forced, but caused by the ejection of hot graphite particles or through auto-ignition due to the large temperatures the gas is subjected to. Following this peak, the system underwent a cooling phase, stabilizing

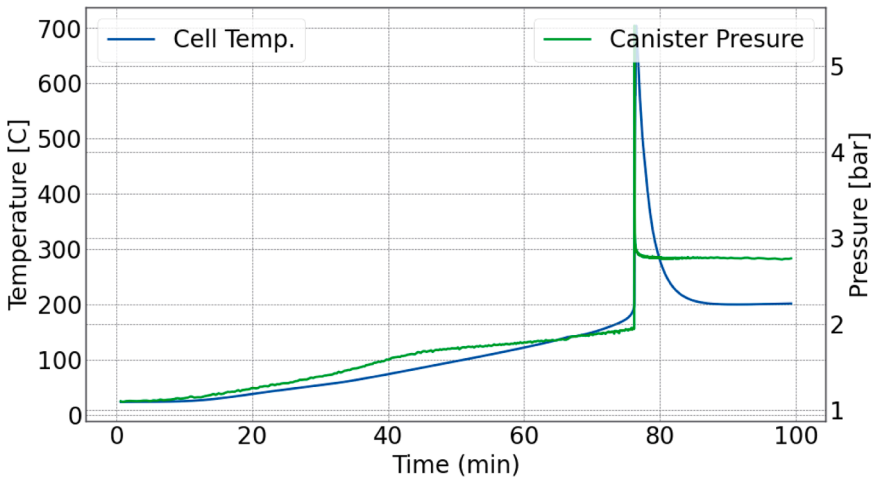

Fig. 4. Transient profiles of cell temperature and internal pressure during thermal runaway test for NMC811 at 100 % SOC.

both temperature and pressure levels.

Further experiments were conducted on three cells of interest to characterize the gas emissions during thermal runaway events. In this series, an inert atmosphere was introduced within the sealed test chamber to prevent combustion reactions, enabling isolation of the gases purely generated from cell decomposition. This setup allows for a direct comparison with the gases emitted under reactive conditions and supports accurate input for computational modeling of TR scenarios. After each test, gas chromatography was employed to analyze the composition of the vented gases. The results are summarized in Fig. 5, which presents the mass fraction of each identified gas under both reactive and inert environments. In both conditions, the main gaseous components were Carbon dioxide (CO_2), Carbon monoxide (CO), and Hydrogen (H_2). Minor components, like methane (CH_4) and ethylene (C_2H_4). Under reactive conditions, CO_2 constituted the largest share (43 %), followed by CO (33 %) and H_2 (22 %), with trace CH_4 and C_2H_2 contributing marginally.

In contrast, the inert atmosphere revealed a lower proportion of CO_2, while CO and H_2 remained prominent. Specifically, CO increased slightly, and CH_4 and C_2H_4 showed higher relative presence than in the reactive case.

The characterization of the gas composition through the inert atmosphere experiments, as it allows depiction of the pyrolysis and decomposition reactions without the eventual oxidation, provides intrinsic vent-gas composition resulting purely from Thermal Runaway reactions. This specific data will serve as initial condition input to the 0D/1D and to determine which amount of gases should be generated by each TR mechanism in the 2D axisymmetric simulations that will later be presented, and assess the combustion process on this information. Gas composition on inert conditions will serve as valuable data for model validation after the TR event.

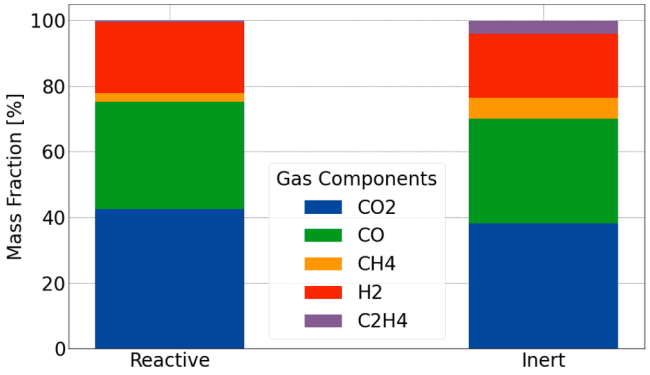

Fig. 5. Gas composition by percentage following thermal runaway of the NMC811 cell at 100 % SOC for inert and reactive atmospheres.

3.2. Analysis of combustion mechanism performance

To assess the predictive capabilities of different combustion mechanisms, a set of homogeneous reactor simulations was performed. For that, the characteristic venting species (CO, CO_2, H_2, CH_4 and C_2H_4) obtained during the inert atmosphere experiments has been input as initial gas concentration in the following calculations. When comparing all the mechanisms, two different Ignition Delay (ID) trends are observed in Fig. 6. Complex mechanisms (Lund, MFL and Gri-Mech 3.0) show similar ID dependency with temperature, depicting auto-ignition times below 1 s under temperatures higher than 850 K and reaching ID times below 0.1 s at temperatures higher than 930 K. On the other hand, the Two Step mechanism shows ID times below 1 s at temperatures higher than 600 K, and below 0.1 s above 650 K. The differences suggest that using simplified mechanisms, although accelerating significantly simulations, could lead to unrealistic results.

These trends are confirmed by analyzing the Laminar Flame Speed (LFS) on premixed in a one-dimensional freely propagating flame configuration flame calculation. The LFS represents the speed at which the air-fuel mixture consumes under ideal conditions. The results are included in Fig. 7. In it, equivalence ratio represents the fuel-to-air-ratio over the stoichiometric fuel-to-air-ratio. Values larger than 1 indicates a fuel-rich mixture, while values lower than 1 implies fuel-lean mixtures.

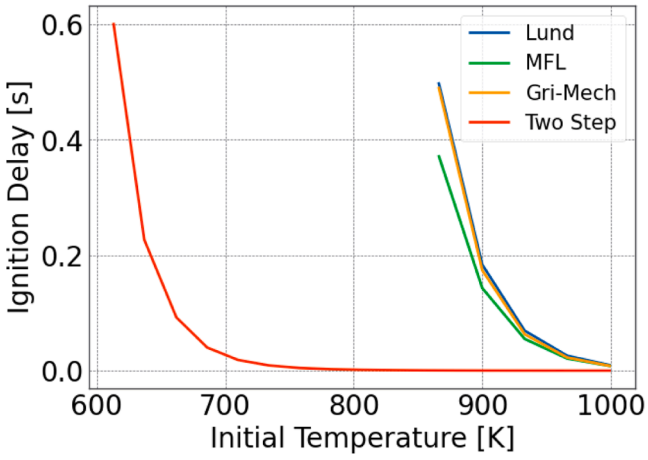

Fig. 6. Ignition delay results for different kinetic mechanisms at different starting temperatures.

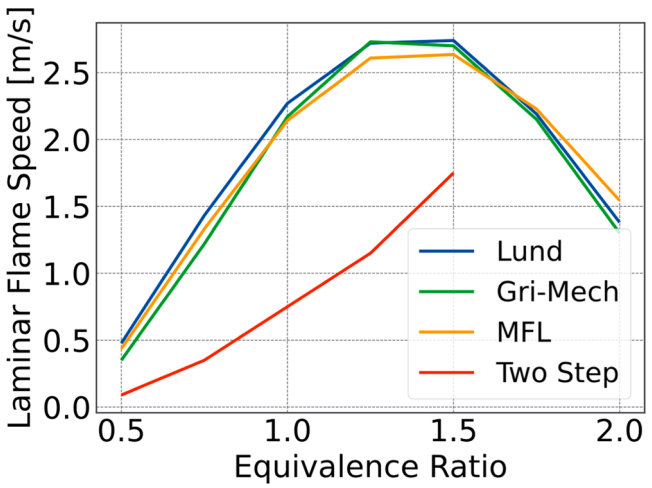

Fig. 7. Laminar flame speed with respect to the equivalence ratio for ambient pressure conditions.

Again, the four proposed kinetic mechanisms are considered. The three complex kinetic mechanisms, (Lund, Gri-mech and MFL) show similar trends, at fuel-lean conditions up to stoichiometric fuel-to-air-ratio. Above that point, slight differences start to arise, showing a better agreement between the Gri-mech and MFL mechanisms, while the Lund mechanism shows slightly lower velocity values. On the other hand, the two-step mechanism, once again, shows completely different trends with respect to the more complex ones, not showing maximum laminar flame speed values for the tested equivalence ratio values, in addition to significantly lower flame speeds.

Although these results have not been experimentally validated, the mechanism from Lund returns similar values to the ones obtained in its original study, in which similar gas compositions were employed. Additionally, in the axisymmetric simulations this information will play a role in the combustion behavior which will be validated through reactive atmosphere experiments.

Based on these first results, it can be easily deducted that the two-step mechanism with a low number of reactions does significantly deviate from the more-complex and TR-dedicated kinetic mechanisms. Thus, the authors do not recommend it for simulating the process of TR fires. Therefore, it was decided to discard this mechanism at this stage of the work. Additionally, despite the MFL mechanism has been served as a reference as a commercial tool, it was decided to not continue with it as the information within it is not available for the user. Therefore, subsequent analysis focuses on the Gri-mech and Lund mechanisms due to their availability.

Under a realistic TR event, LIBs would be enclosed within a module packaging. As the gas is being ejected, mixed with available oxygen, and burned, the pressure inside the packaging will increase. For that reason, LFS analysis was also extended to a set of initial ambient pressures under which the ejection of TR gases could take place. The results are shown in Fig. 8, which presents the ratio of LFS obtained with both mechanisms. The trend observed in Fig. 7 is followed throughout the different initial pressures, showing very similar results in close-to-stoichiometric conditions, and some deviations under lean and rich conditions. Differences aggravate with larger initial pressure values and reach up to a 50 %.

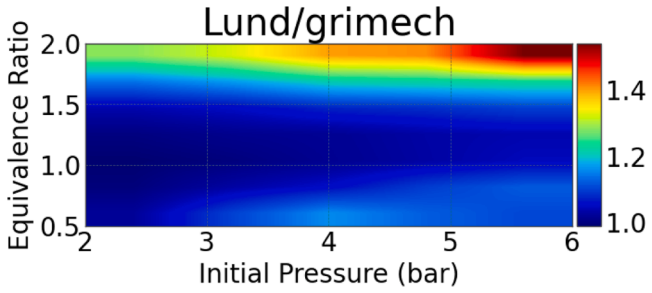

Fig. 8. Laminar Flame Velocity Ratio between Gri-Mech and Lund mechanisms for different Equivalence ratio and Initial pressures.

As already depicted, both Gri-Mech and Lund mechanisms behave in similar ways for the different analysis performed during this study. Nonetheless, Lund mechanism has a significant larger number of possible species, some of them that could act as fuel during a TR fire, such as different electrolyte or HF. HF could be an additional gaseous emission that is expected from TR events. Nonetheless, its contribution towards combustion is expected to be low enough to not considering it [45]. Even though, it can be an implementation for future work, hence the 2-D axisymmetric studies have been carried out with "Lund" mechanism as it considers these possibilities.

3.3. Reduction of the original mechanism

The mechanism provided by Nilsson et al. [1] ("Lund") is composed of 614 species and a total of 3642 reactions, which makes it heavy for large-scale simulations. Thus, including the mechanism in its original state to the 2D axisymmetric CFD, although having a reduced number of computational cells, would imply significant computational cost when resolving kinetics. For that purpose, prior to its implementation, the mechanism has been reduced through CHEMKIN Pro mechanism reducer. The tool has been set up with several objective functions through a pre-mixed gaseous jet reactor. It was aimed to maintain the same composition of combustion products once the solution has converged, in addition to maintaining the same laminar flame speed. To ensure that the combustion process is properly captured, some middle species have been also set to be similar to the original mechanism, particularly the OH, as it is a good combustion indicator [46]. The mechanism reduction has been done based on several optimization procedures, starting with a Direct Relation Graph with Error Propagation (DRGEP), following a Direct Relation Graph method (DRG) [47] and a Direct Relation Graph Method with Path Flux Analysis (DRGPFA) [34]. A maximum error of 10 % on the selected objectives has been allowed during the procedure, while the CHEMKIN Pro default parameters have been left for the DRG and DRGPFA optimization. Once the mechanism reduction has been completed, the resulting skeletal mechanism has been compared not only against the target objectives but also against ID values to ensure the highest precision for several initial pressure conditions. Fig. 9 is the result of this comparison for ID and LFS, depicting the low errors of the skeletal mechanism solutions compared to the original mechanism. Regarding ID, it can be seen that the error at all the equivalence ration is quite below 0.1 %. In terms of LFS, the differences are higher, specially between equivalence ratio 1.0 and 1.5,

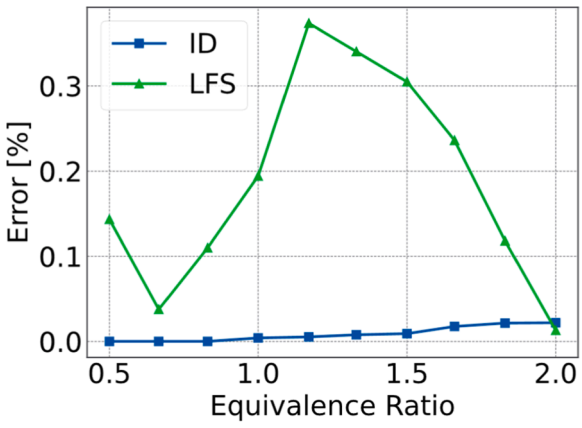

Fig. 9. Error on the Ignition Delay (ID) and Laminar Flame Speed (LFS) for the reduction of the master mechanism.

although being below 0.4 % in all cases. This confirms that the reduced version, containing 128 species (79.2 % reduction) and a total of 794 reactions (78.2 % reduction), satisfies the overall behavior of the original mechanism and is suitable for its implementation in high-dimensional simulations without affecting accuracy. The skeletal mechanism obtained is provided through Supplementary Material.

3.4. Implementation of the reduced mechanism into the three-dimensional model

Simulations have been run to replicate a heating ramp tests carried out experimentally. Not only the achieved reduced mechanism, but also the original one to further check their similarity under high-dimensional simulations. The gas composition extracted from inert ARC tests have been included into the venting model to represent the un-altered species being ejected during the TR event without any combustion process taking place. As the computational model does not account for the heat transfer from the ARC walls to the closed-volume walls, the temperature of the outer surface of the closed-volume walls (measured in experiments) has been introduced as boundary condition of the model.

Validation comprises coupled TR, venting and combustion models thanks the different experimental data collected. The temperature achieved by the cell and the pressure of the closed-volume are shown in Fig. 10. The heat transfer dynamics during the heat up phase are underpredicted on the proposed computational model as Jelly-Roll properties were taken from literature, probably showing variations with the actual values. The maximum associated deviation is 10 % until the highly exothermic event. Thermal runaway triggering time is also well captured. This value has been considered to be the point in which the temperature time derivative of the cell reaches 100 °C/min. On the experimental data this is reached at 77.7 min, while for the computational model it is reached at 78.9 min, a deviation of 1.5 %. Regarding the peak temperatures, 690 °C is achieved on the experiment against the 640 °C on the model. These differences can also be observed on other TR modelling studies in which differences up to 50 °C are reported [37]. Regarding the venting and combustion sub-model, they are validated throughout the pressure signal captured during the experimental campaign and the comparison between the experimental and computational gas composition after the combustion event. The pressure rise before the TR event is caused by the heat up of the reactive atmosphere within the closed-volume. Once TR is triggered, and large amounts of gases start to be ejected and eventually combusted, additional pressure rise is observed, much more abrupt and short in time caused by these combined events. In overall terms, the considered model is also capable of predicting this set of events in a macroscopic way, matching the data that was retrieved through experimental means on the closed-volume setup. Considering all this, it can be stated that the model can reproduce the phenomena under ARC—HWS closed-volume configuration with high accuracy. Thus, the methodology could be extended to more realistic closed-volume situations.

A more precise analysis of the exothermic process can be done by computing the heating rate based on the temperature of the cell, which is shown in Fig. 11. As observed, the initial heating phase (up to 200 °C) is appropriately captured. The starting of the exothermic event (100 °C/min) is observed at temperatures of 200 °C on the experiment and 220 °C for the presented model. During the highly exothermic phase, both methods show similar heating rate values with the subsequent decay at above 500 °C. As it was expected, the experiment provides curves up to almost 690 °C while the model stops the exothermic process at 640 °C.

The venting velocity calculated during the simulation by the implemented model is presented in Fig. 12. When the heating rate increases exponentially, a significant amount of gases start to be ejected. During the initial phase, a continuously increasing jelly-roll volume goes into TR. This is associated to an increasing TR propagation surface inside the cell, generating large gas quantities and hence depicting large velocities up to 300 m/s, achieving choked conditions at the LIB nozzle section. After that, the TR propagation front within the cell achieves stable conditions, the velocity goes down to around 60 m/s until little active material is left within the reacting solid, and the front surface is reduced to null velocity conditions. In the computational model, from 450 °C to 640 °C no gas is ejected as no gaseous mass is associated to the cathode reaction, the one that takes place at high temperature values.

The characteristics of the combustion process will be analyzed next. In Fig. 13 the temperature contours are shown. In it, two different phenomena can be described. On the one hand, the combustion process of the ejected gases on the gaseous domain. In the first half of the ejection process (Fig. 13a–e) the flame is detached from the LIB due to

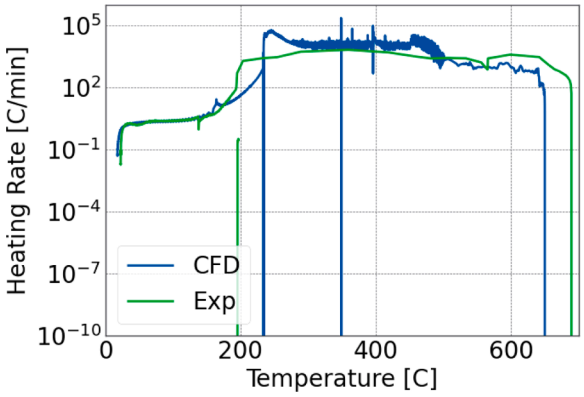

Fig. 11. Heating rate comparison between methods.

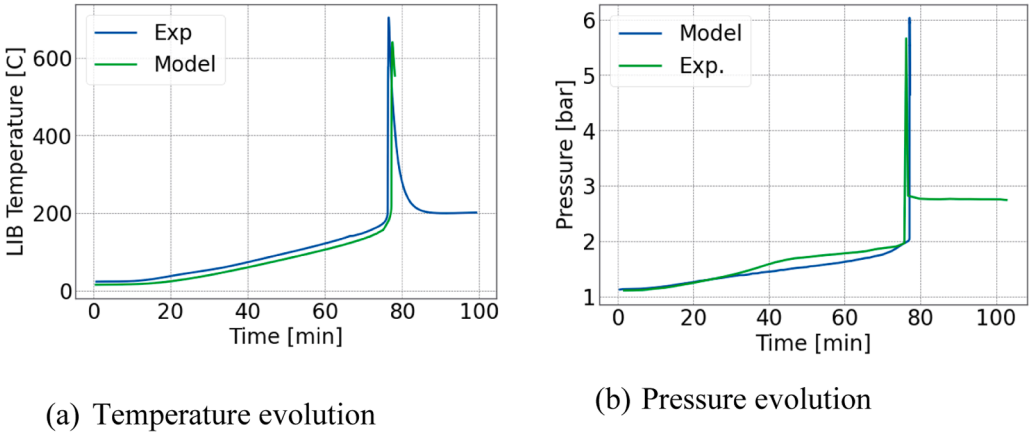

Fig. 10. Comparison between methods of the LIB temperature and closed-volume pressure.

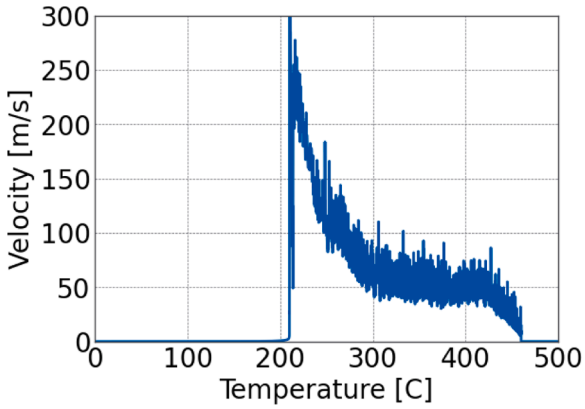

Fig. 12. Velocity profile calculated by the described venting model.

the high velocities that are being calculated. Once the velocities stabilize to values around 50 m/s, the flame front travels back to the LIB inlet section (Fig. 13f and g). During the initial combustion process, high temperatures are observed within the flame front, close to 2500 °C. These temperatures progressively reduces as the availability of the O_2 is decreased throughout the event, when the flame front is displaced towards the lower region of the closed-volume, near the solid LIB holder geometry. The second effect that can be described from these contours is the exothermic process the LIB is suffering from the degradation of the internal reactions. Initially, the TR is taking place in the upper region of the LIB. The generated heat is transferred due to conduction throughout the LIB. The orthotropic conductivity of the cell (larger in the axial and tangential directions than in the radial), it propagates faster in the axial direction, reaching temperatures close to 650 °C, as expected from previous results. Both the TR and combustion events are fast in time, with the combustion process happening in less than 2 s.

The flame front can be directly visualized through the representation of the hydroxyl radical (OH). This radical is highly reactive and is only present on regions where the main oxidation reactions are present. Hence it allows to know where the flame front is present. This mass fraction contour representation is present in Fig. 14. As it happened with the temperature contours, high mass fractions are presents in the sequence where high inlet velocities are calculated. The flame front does not only extend up to the upper closed-volume surface, but it is deflected by these walls to the sides. Two combustion regions appear on the wall laterals (Fig. 14c–f) in which fuel is still being mixed with available oxygen. Once the upper region of the volume has totally consumed the available oxygen, a clear flame-front is generated that displaces towards the bottom part of the volume. As this is still taking place, the OH mass fraction keeps decreasing in magnitude, highly associated to the corresponding decrease of temperatures shown in Fig. 13.

As mentioned, some analysis is done on both skeletal (reduced) and original kinetic mechanism. The results to be discussed include a comparison between them. The heat released profile has been represented in Fig. 15, together with the cumulative heat released. The evolution with the LIB temperature, not the time, has been included to analyse possible resembling with other characteristic TR data. Regarding this topic, both curves overlap almost perfectly, further indicating the applicability of the proposed reduction process for battery fires. The shape of the Heat Release Rate (HRR) curve is highly related to the calculated velocity curve from Fig. 12. At instants where the velocity was calculated to be higher than ~80 m/s provides HRR higher than 50 kW, and once the velocity reaches some more steady-state condition, the HRR curve stabilizes at around 12.5 kW. The combustion process at the end of the TR event shows a cumulative energy release of 65 kJ, as provided by the image.

The energy released by the cell has been calculated based on the different energy sources that are present during a TR event. Three

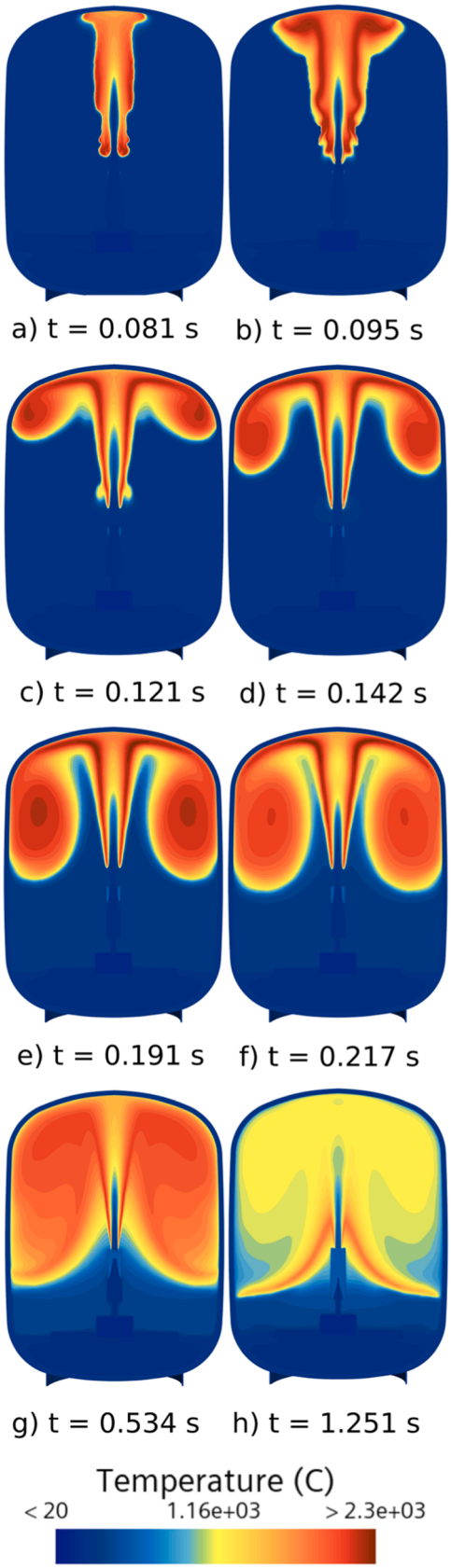

Fig. 13. Time sequence of the temperature contour during the combustion process.

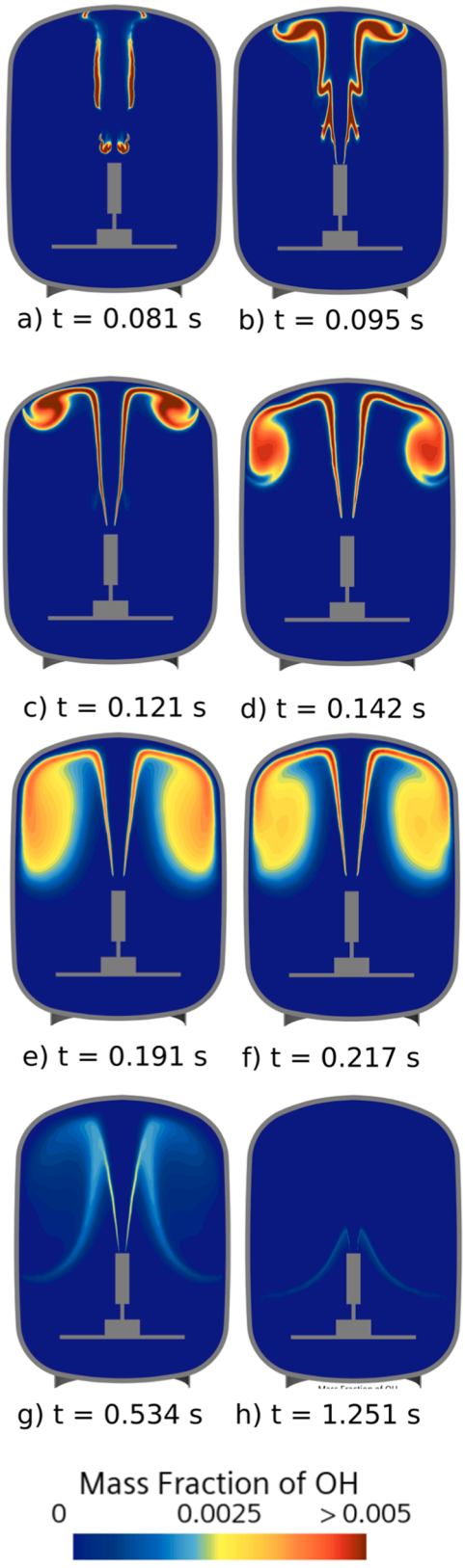

Fig. 14. Time sequence of the OH contours during the combustion process.

different contributions are considered, first the exothermic process that the cell itself suffers, which is calculated based on Eq. (15); the energy due to the ejection of the gases, which has been calculated through Eq. (16) from [48]. In it, the U terms stand for the internal energy of the corresponding gases at each of the indicated temperatures. The third

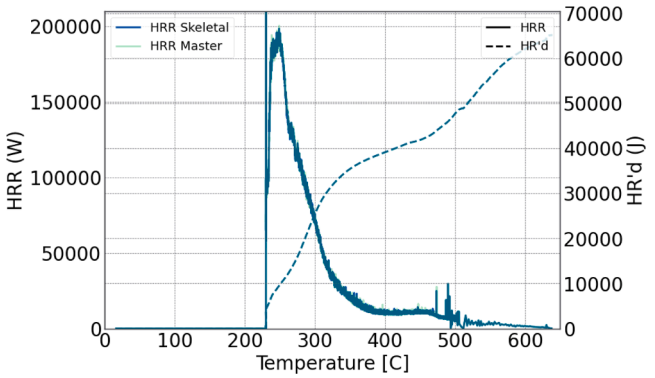

Fig. 15. Heat Release Rate and cumulative Heat Release for the combustion model.

term is the energy release due to the combustion of the gases, which has already been indicated.

$$E_{LIB} = m_{LIB} C_p \Delta T \tag{21}$$

$$E_{venting} = \left(U_{vent,T_{LIB}} + R_{gas} T_{LIB} - U_{vent,T_{gas}}\right) dm/dt \tag{22}$$

The value of the released energies has been included in Table 4. In it, the dimensionless energy release factor has been included, which accounts for the ratio of energy released during TR compared to the energy that is stored through electro-chemical means. It is observed that the combustion energy accounts for the 70 % of the released energy, being a 20 % due to the exothermic event on the LIB, and the remaining in terms of gas venting. This implies that during this event, the cell is capable of releasing around twice of the stored energy if a LIB suffers TR conditions.

When it comes to the species resulting from the combustion process, the temporal and final composition of the gases can be analyzed. This information is located in Fig. 16. Regarding Fig. 16a, it depicts the temporal evolution of the species during the combustion process. The species that could be experimentally measured have been represented. This representation has been also used to completely validate the skeletal mechanism achieved against the original one. On that matter, both temporal curves are overlapped, hence once more indicating the suitability of the reduced kinetic mechanism for TR fires. On the other hand, it can be observed how initially all the gaseous reactive species are being burned, as their mass fraction does not increase. It is once the available oxygen starts to become a limitation during the combustion process where the start to be represented on the temporal evolution. Most visible case is the CO species, which after 0.2 s starts to significantly be present in the domain, indicating its incapability to further reduce into CO_2. Regarding the final mass fraction, it can be compared with the experimental mass fraction obtained, and once again with the skeletal mechanism. Once more, no significant differences arise from the two employed kinetic mechanisms. With respect to the comparison with experimental data, similar mass fractions of CO_2 are achieved, while certain differences appear on the CO and H_2. These differences are attributed to the lower available oxygen on the simulation model, as the flame once it reaches the LIB holder extinguishes, while experimentally, this LIB holder is a perforated plate that allows the flame to go through,

Table 4
Energy considerations during TR.

Parameter	Value
Cell energy released	22.5 kJ
Gases energy released	4.6 kJ
Combustion energy released	64.8 kJ
Electrochemical energy stored	41.47 kJ
Energy release factor	2.22

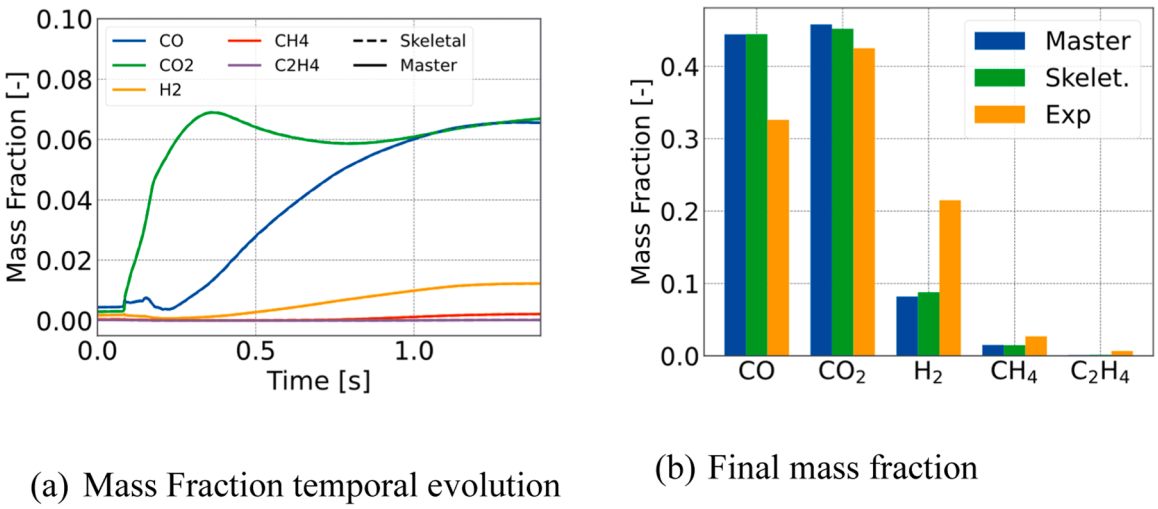

(a) Mass Fraction temporal evolution

(b) Final mass fraction

Fig. 16. Temporal evolution and end-of-combustion mass fractions.

employing the oxygen below the holder to further burn the gases.

In addition to achieving a skeletal model that faithfully replicates the behavior and trends of the master combustion mechanism, it provides shorter simulation times due to the lower number of species whose combustion kinetics and transport equations do not need to be solved anymore. The computational cost on performing 2D-axisymmetric simulations has been calculated and compared across the master and skeletal mechanisms. A total of 1425 CPU-h was needed to perform the simulation with the master mechanism, while 745 CPU-h were employed for the skeletal mechanism. Same number of CPUs were used for each case (4 Intel Xeon Gold 6154), hence showing a speedup of 1.91 by using the skeletal mechanism, reducing by half the needed computation time.

4. Conclusions

This study presented an integrated experimental and computational investigation of gas-phase combustion during thermal runaway in commercial cylindrical NMC811 lithium-ion cells for battery fire risk modeling. The proposed model can be used to predict the consequences of a TR event under closed-environment conditions, as the ones found on battery module casings, hence providing a useful tool to design such environments to sustain the temperature and pressure conditions due to a TR fire. The key findings of this work are:

1. Accelerating rate calorimetry experiments on NMC811 cells under inert and reactive conditions revealed significant differences in vented gas compositions. In reactive environments, CO2 (43 %), CO (33 %), and H2 (22 %) dominated, while inert environments showed higher levels of CH4 and C2H4. The gas composition obtained through the inert conditions has been directly introduced into the computational framework as it represents purely the outcomes from the Thermal Runaway event without the eventual oxidation after its ejection.
2. A comparative evaluation of multiple combustion mechanisms demonstrated that detailed kinetics are essential for accurately predicting ignition delay and flame propagation in battery vent gases, with simplified models showing deviations exceeding 40 % at high-pressure conditions.
3. The comprehensive Lund mechanism was successfully reduced by 80 % (from 614 species and 3642 reactions to 128 species and 794 reactions) while maintaining prediction accuracy within 10 % for critical combustion parameters.
4. The reduced mechanism, integrated into a 2D axisymmetric CFD model, accurately reproduced experimental temperature profiles (maximum 704 °C), pressure evolution (5.70 bar), and flame structure. It helped reduce the computational cost by a factor of 2.
5. Results revealed that high venting velocities (>300 m/s) led to flame detachment, with flame front propagation dynamics strongly influenced by oxygen availability and a total combustion energy release of 65 kJ.

The presented coupled experimental-computational methodology allows direct assessment on the conditions under which combustion process could be taking place due to auto-ignition sources. Through the selection of the Lund combustion mechanism, this analysis has become possible at cell level studies, maintaining the fidelity of the model.

Future work employing the developed tools during this work could be aimed towards analysing the contribution of the combustion process in the TRP phenomenon and compare the different heat transfer pathways that could take place. The model does not include the venting of electrolytes, neither the inclusion of particles that could eventually ignite the flammable mixture; hence ignition mechanism could be assessed.

CRediT authorship contribution statement

Antonio García: Supervision, Methodology, Conceptualization. **Carlos Micó:** Writing – review & editing, Writing – original draft, Supervision, Methodology, Investigation, Formal analysis, Conceptualization. **Javier Marco-Gimeno:** Writing – review & editing, Writing – original draft, Validation, Methodology, Investigation, Formal analysis, Data curation, Conceptualization. **Imad Elkourchi:** Writing – review & editing, Writing – original draft, Software, Investigation.

Declaration of competing interest

The authors declare that they have no known competing financial interests or personal relationships that could have appeared to influence the work reported in this paper.

Acknowledgment

This research has been funded through CIAICO/2023/017, by Conselleria de Educación, Cultura, Universidades y Empleo

Supplementary materials

Supplementary material associated with this article can be found, in the online version, at doi:10.1016/j.jaecs.2025.100375.

Data availability

Data will be made available on request.

References

[1] Bugryniec PJ, Resendiz EG, Nwophoke SM, Khanna S, James C, Brown SF. Review of gas emissions from lithium-ion battery thermal runaway failure — Considering toxic and flammable compounds. J Energy Storage 2024;87:111288. https://doi.org/10.1016/J.EST.2024.111288.

[2] Wang Q, Mao B, Stoliarov SI, Sun J. A review of lithium ion battery failure mechanisms and fire prevention strategies. Prog Energy Combust Sci 2019;73:95–131. https://doi.org/10.1016/J.PECS.2019.03.002.

[3] Jia Z, Wang S, Qin P, Li C, Song L, Cheng Z, Jin K, Sun J, Wang Q. Comparative investigation of the thermal runaway and gas venting behaviors of large-format LiFePO4 batteries caused by overcharging and overheating. J Energy Storage 2023;61:106791. https://doi.org/10.1016/J.EST.2023.106791.

[4] Henriksen M, Vaagsaether K, Lundberg J, Forseth S, Bjerketvedt D. Laminar burning velocity of gases vented from failed Li-ion batteries. J Power Source 2021;506:230141. https://doi.org/10.1016/J.JPOWSOUR.2021.230141.

[5] Yu R, Liu J, Liang W, Law CK, Wang H, Ouyang M. On explosion limits of NCA battery vent gas. Proc Combust Inst 2023;39:3031–40. https://doi.org/10.1016/J.PROCI.2022.11.010.

[6] Zhang Y, Zhao H, Wang G, Gao X, Ping P, Kong D, Yin X. Effect of flame heating on thermal runaway propagation of lithium-ion batteries in confined space. J Energy Storage 2024;78:110052. https://doi.org/10.1016/J.EST.2023.110052.

[7] Kim J, Mallarapu A, Finegan DP, Santhanagopalan S. Modeling cell venting and gas-phase reactions in 18650 lithium ion batteries during thermal runaway. J Power Source 2021;489:229496. https://doi.org/10.1016/J.JPOWSOUR.2021.229496.

[8] Voigt S, Sträubig F, Kwade A, Zehfuß J, Knaust C. An empirical model for lithium-ion battery fires for CFD applications. Fire Saf J 2023;135:103725. https://doi.org/10.1016/J.FIRESAF.2022.103725.

[9] Ling Z, Lu L, Zeng X, Kuang M, Ling B, Gao C, Zhou C. Ethylene combustion performance with varying the N2 content in a porous burner. Energy 2023;262:125321. https://doi.org/10.1016/J.ENERGY.2022.125321.

[10] Xie W, Zhang L. Experimental study on thermal runaway and venting gas explosion hazards in prismatic lithium-ion batteries at different states of charge. Process Safe Environ Protect 2025;198. https://doi.org/10.1016/j.psep.2025.107118.

[11] Li Z, Cheng Y, Ding K, Wang S, Yu Y, Wang J, Cheng Z, Jin K, Mei W, Wang Q. Experimental investigation on thermal runaway propagation of lithium-ion battery module under different trigger locations. Process Safe Environ Protect 2025;198. https://doi.org/10.1016/j.psep.2025.107166.

[12] Lin C, Yan H, Qi C, Liu Z, Liu D, Liu X, Lao L, Li Z, Sun Y. Thermal runaway and gas production characteristics of semi-solid electrolyte and liquid electrolyte lithium-ion batteries: a comparative study. Process Safe Environ Protect 2024;189:577–86. https://doi.org/10.1016/j.psep.2024.06.111.

[13] Wang H, Xu H, Zhang Z, Wang Q, Jin C, Wu C, Xu C, Hao J, Sun L, Du Z, Li Y, Sun J, Feng X. Fire and explosion characteristics of vent gas from lithium-ion batteries after thermal runaway: a comparative study. ETransportation 2022;13:100190. https://doi.org/10.1016/J.ETRAN.2022.100190.

[14] Wang G, Ping P, Zhang Y, Zhao H, Lv H, Gao X, Gao W, Kong D. Modeling thermal runaway propagation of lithium-ion batteries under impacts of ceiling jet fire. Process Safe Environ Protect 2023;175:524–40. https://doi.org/10.1016/j.psep.2023.05.047.

[15] Xu L, Wang S, Li Y, Li Y, Sun J, Zhao F, Wang H, Wang Y, Xu C, Feng X. Thermal runaway propagation behavior and gas production characteristics of NCM622 battery modules at different state of charge. Process Safe Environ Protect 2024;185:267–76. https://doi.org/10.1016/j.psep.2024.03.011.

[16] Wang Q, Wang H, Xu C, Jin C, Wang S, Xu L, Ouyang J, Feng X. Multidimensional fire propagation of lithium-ion phosphate batteries for energy storage. ETransportation 2024;20:100328. https://doi.org/10.1016/J.ETRAN.2024.100328.

[17] Jie D, Baohui C, Jiazheng L, Tiannian Z, Chuanping W. Thermal runaway and combustion characteristics, risk and hazard evaluation of lithiumiron phosphate battery under different thermal runaway triggering modes. Appl Energy 2024:368. https://doi.org/10.1016/j.apenergy.2024.123451.

[18] Dong W, Xu C, Huang W, Peng Y, Zhang M, Wang H, Jin C, Fan Y, Feng X. Dynamic simulation on the deformation of the battery module under thermal runaway propagation based on internal pressure. Process Safe Environ Protect 2025;195. https://doi.org/10.1016/j.psep.2024.12.114.

[19] Fan R, Wang Z, Lu Y, Lin C, Guo W. Numerical analysis on the combustion characteristic of lithium-ion battery vent gases and the suppression effect. Fuel 2022;330. https://doi.org/10.1016/j.fuel.2022.125450.

[20] Nilsson EJ, Brackmann C, Tidblad AA. Evaluation of combustion properties of vent gases from Li-ion batteries. J Power Source 2023;585:233638. https://doi.org/10.1016/J.JPOWSOUR.2023.233638.

[21] Baird AR, Archibald EJ, Marr KC, Ezekoye OA. Explosion hazards from lithium-ion battery vent gas. J Power Source 2020;446:227257. https://doi.org/10.1016/J.JPOWSOUR.2019.227257.

[22] Cellier A, Duchaine F, Poinsot T, Okyay G, Leyko M, Pallud M. An analytically reduced chemistry scheme for large eddy simulation of lithium-ion battery fires. Combust Flame 2023;250:112648. https://doi.org/10.1016/J.COMBUSTFLAME.2023.112648.

[23] Vendra CMR, Shelke AV, Buston JEH, Gill J, Howard D, Read E, Abaza A, Cooper B, Wen JX. Numerical and experimental characterisation of high energy density 21700 lithium-ion battery fires. Process Safe Environ Protect 2022;160:153–65. https://doi.org/10.1016/J.PSEP.2022.02.014.

[24] Wang G, Ping P, Zhang Y, Zhao H, Lv H, Gao X, Gao W, Kong D. Modeling thermal runaway propagation of lithium-ion batteries under impacts of ceiling jet fire. Process Safe Environ Protect 2023;175:524–40. https://doi.org/10.1016/J.PSEP.2023.05.047.

[25] Kong D, Wang G, Ping P, Wen J. A coupled conjugate heat transfer and CFD model for the thermal runaway evolution and jet fire of 18650 lithium-ion battery under thermal abuse. ETransportation 2022;12:100157. https://doi.org/10.1016/J.ETRAN.2022.100157.

[26] Peng R, Kong D, Ping P, Wang G, Gao X, Lv H, Zhao H, He X, Zhang Y, Dai X. Thermal runaway modeling of lithium-ion batteries at different scales: recent advances and perspectives. Energy Storage Mater 2024;69:103417. https://doi.org/10.1016/J.ENSM.2024.103417.

[27] Henriksen M, Vaagsaether K, Lundberg J, Forseth S, Bjerketvedt D. Simulation of a premixed explosion of gas vented during Li-ion battery failure. Fire Saf J 2021;126:103478. https://doi.org/10.1016/J.FIRESAF.2021.103478.

[28] Li X, Yang W, Yin L, Zhang S, Wu Y, Mao Y, Jia W, Wu D, Chen K, Yuan L, Zhou X, Li C. Advancing lithium battery safety: introducing a composite phase change material with anti-leakage and fire-resistant properties. ETransportation 2025;23:100387. https://doi.org/10.1016/J.ETRAN.2024.100387.

[29] Meng X, Li S, Fu W, Chen Y, Duan Q, Wang Q. Experimental study of intermittent spray cooling on suppression for lithium iron phosphate battery fires. ETransportation 2022;11:100142. https://doi.org/10.1016/J.ETRAN.2021.100142.

[30] Wang G, Ping P, Kong D, Peng R, He X, Zhang Y, Dai X, Wen J. Advances and challenges in thermal runaway modeling of lithium-ion batteries. The Innovation 2024;5:100624. https://doi.org/10.1016/J.XINN.2024.100624.

[31] GRI-Mech 3.0, (n.d.). http://combustion.berkeley.edu/gri-mech/version30/text30.html#cite (accessed May 5, 2025).

[32] Ansys Model Fuel Library | Fuel Simulation Models, (n.d.). https://www.ansys.com/products/fluids/ansys-model-fuel-library (accessed May 5, 2025).

[33] Westbrook CK, Dryer FL. Chemical kinetic modeling of hydrocarbon combustion. Prog Energy Combust Sci 1984;10:1–57. https://doi.org/10.1016/0360-1285(84)90118-7.

[34] Castellani S, Nassini PC, Andreini A. Optimization of a two-step CH4/air reaction mechanism in a CO2-enriched environment for high-fidelity combustion simulations. Front Mech Eng 2023;9:1240761. https://doi.org/10.3389/FMECH.2023.1240761/BIBTEX.

[35] Pettersson O, Magnusson S, Thor J. Fire engineering design of steel structures. 1976. https://portal.research.lu.se/files/5989339/1245743.pdf (accessed August 11, 2025.

[36] Chen SC, Wan CC, Wang YY. Thermal analysis of lithium-ion batteries. J Power Source 2005;140:111–24. https://doi.org/10.1016/J.JPOWSOUR.2004.05.064.

[37] H.K. Versteeg, W. Malalasekera, An introduction to Computational Fluid Dynamics Second Edition, n.d. www.pearsoned.co.uk/versteeg.

[38] D. Wilcox, Turbulence modeling for CFD, 1998. http://sutlib2.sut.ac.th/sut_contents/H133907.pdf (accessed May 20, 2025).

[39] Modelling Li-ion cell thermal runaway triggered by an internal short circuit device using an efficiency factor and arrhenius formulations, (n.d.). https://doi.org/10.1149/2.0341704jes.

[40] Ren D, Liu X, Feng X, Lu L, Ouyang M, Li J, He X. Model-based thermal runaway prediction of lithium-ion batteries from kinetics analysis of cell components. Appl Energy 2018;228:633–44. https://doi.org/10.1016/J.APENERGY.2018.06.126.

[41] A. Gil, J. Monsalve-Serrano, J. Marco-Gimeno, C. Guaraco-Figueira, Numerical model of the heat-wait and seek and heating ramp protocol for the prediction of thermal runaway in lithium-ion batteries, (2025). https://doi.org/10.4271/2025-01-8127.

[42] He D, Wang J, Peng Y, Li B, Feng C, Shen L, Ma S. Research advances on thermal runaway mechanism of lithium-ion batteries and safety improvement. Sustain Mater Technolog 2024;41:e01017. https://doi.org/10.1016/J.SUSMAT.2024.E01017.

[43] Fang YJ, Qian JM. Isobaric vapor-liquid equilibria of binary mixtures containing the carbonate group -OCOO. J Chem Eng Data 2005;50:340–3. https://doi.org/10.1021/JE049859C/ASSET/IMAGES/LARGE/JE049859CF00005.JPEG.

[44] Kwak E, hyeong Kim J, Jeong J, Oh KY. Multiphysics-informed thermal runaway model for estimating the pressure evolution induced by the gas formation in a lithium-ion battery. Appl Therm Eng 2024;246:122941. https://doi.org/10.1016/J.APPLTHERMALENG.2024.122941.

[45] Nilsson EJK, Tidblad AA. Gas emissions from lithium-ion batteries: a review of experimental results and methodologies. Batteries 2024;10. https://doi.org/10.3390/BATTERIES10120443. Page 443 10 (2024) 443.

[46] GRI-Mech 3.0, (n.d.). http://combustion.berkeley.edu/gri-mech/version30/text30.html (accessed May 22, 2025).

[47] Lu T, Law CK. A directed relation graph method for mechanism reduction. Proc Combust Inst 2005;30:1333–41. https://doi.org/10.1016/J.PROCI.2004.08.145.

[48] Martin J, Monsalve-Serrano J, Micó C, Elkourchi I. Thermal model for the analysis of the Thermal runaway in lithium-ion batteries using accelerating rate calorimetry. SAE Techn Pap 2023. https://doi.org/10.4271/2023-24-0162.